



Contents lists available at ScienceDirect

Remote Sensing of Environment

journal homepage: www.elsevier.com/locate/rse

Pollen in the Baltic Sea as viewed from space

Chuanmin Hu^{a,*}, Lin Qi^{b,c}, David C. English^a, Menghua Wang^b, Karlis Mikelsons^{b,c}, Brian B. Barnes^a, Magdalena M. Pawlik^d, Dariusz Ficek^d^a College of Marine Science, University of South Florida, St. Petersburg, FL, USA^b National Oceanic and Atmospheric Administration, Center for Satellite Applications and Research, College Park, MD, USA^c Global Science and Technology, Inc., Greenbelt, MD, USA^d Pomeranian University in Stupsk, Institute of Biology and Earth Sciences, Stupsk, Poland

ARTICLE INFO

Edited by Dr. Marie Weiss

Keywords:

Pollen
Marine litter
Plastics
cyanobacteria
Baltic Sea
Gulf of Bothnia
Gulf of Finland
Gdansk Bay
Gotland
MODIS
VIIRS
OLCI
MERIS
MSI
Sentinel-2
Sentinel-3
Carbon cycle
Bio-optics
Climate change

ABSTRACT

Multi-sensor satellite images often show recurrent image slicks in the Baltic Sea. Based on historical reports, laboratory experiments, and spectral diagnostics, these image slicks are determined to be caused by pine (*Pinus sylvestris*) pollen aggregations as opposed to surface scums of cyanobacteria or other floating matters. This attribution is because the reflectance spectral shapes of these image slicks resemble those of pollen grains, which are all different from other floating matters. They all show rapid reflectance increase from ~400 to ~500 nm, beyond which the reflectance shape appears to plateau. During the 22-year period of 2000–2021, satellite images indicated large amounts of pollen grains in 14 years, with the earliest day being May 10 (in 2000) and the latest day being June 16 (in 2006). The longest duration in a single year is 22 days, from May 12 to June 2 of 2018. The waters containing pollen grains have expanded significantly in recent years, encompassing nearly the entire Baltic Sea. Because pollen grains contain a significant amount of carbon and have distinctive optical properties from other particles, these findings have significant implications on carbon sequestration, marine ecology, bio-optics, ocean color calibration/validation, and remote sensing of marine debris.

1. Introduction

The Baltic Sea is a tideless semi-enclosed marginal sea bordered by nine countries: Denmark, Estonia, Finland, Germany, Latvia, Lithuania, Poland, Russia, and Sweden, all rich in pine trees and other conifer plants (Fig. 1). The southern and southeastern coasts are dominated by till materials, while hard-bottom and rocky shores are typical along the northern coasts (Schiewer, 2008). Winds are typically strong, with a 50-year average of 7.5 m s^{-1} and predominant westerly or easterly directions in the southern Baltic (Zhang et al., 2011). The hydrodynamic forcing is dominated by wind-driven currents and waves at different scales. While blooms of diatoms and cyanobacteria occur annually in

spring and summer (Kahru et al., 2016, 2020), respectively, allochthonous materials from terrestrial runoff and wind-induced deposition are also abundant, leading to typical Case II waters according to the classical definition of Morel and Prieur (1977) (Gordon and Morel, 1983; Antoine et al., 2014).

The biology, ecology, geology, and physics of the Baltic Sea have been studied extensively using a variety of means including satellite remote sensing (Bradtke, 2021; Ostrowska et al., 2022). These include optical characterization to understand how inherent optical properties (IOPs, absorption, scattering) and apparent optical properties (AOPs, reflectance, light attenuation) are influenced by various forms of particulate and dissolved matters such as phytoplankton, organic detrital

* Corresponding author.

E-mail address: huc@usf.edu (C. Hu).<https://doi.org/10.1016/j.rse.2022.113337>

Received 15 May 2022; Received in revised form 20 October 2022; Accepted 28 October 2022

Available online 8 November 2022

0034-4257/© 2022 The Authors. Published by Elsevier Inc. This is an open access article under the CC BY-NC license (<http://creativecommons.org/licenses/by-nc/4.0/>).

particles, inorganic particles (minerals), and colored dissolved organic matter (Berthon and Zibordi, 2010; Kowalczuk et al., 2010; Woźniak et al., 2016). These optically active constituents (OACs) are not unique to the Baltic Sea, but they are found in nearly all coastal and inland waters around the world.

In addition to the above OACs, several recent studies (Pawlik and Ficek, 2016, 2021; Lienart et al., 2022) also reported pine (*Pinus sylvestris*) pollen grains in coastal waters of the southern Baltic Sea (Gdansk Bay near Poland) and in a nearshore site near Stockholm University (Sweden), respectively (Fig. 1). Pawlik and Ficek (2016 & 2021) further used a Laser In-Situ Scattering and Transmissometry (LISST)-100× instrument to determine the size distribution of pine pollen grains collected from Polish coastal waters, whose equivalent diameters were found to vary between 29.1 and 78.4 μm. These reports have significant implications on optics, remote sensing, ecology, and carbon science at a local scale. For example, Lienart et al. (2022) showed that pine pollen in the Baltic Sea may serve as a significant food source for local invertebrates. Laboratory measurement of *Pinus sylvestris* pollen grains showed 49.5% carbon and 1.4% nitrogen in pollen dry mass (Rösel et al., 2012). Therefore, pine pollen may also be a significant carbon source to the Baltic Sea at a local scale.

However, all these studies reported pollen grains only in coastal waters (up to 10–20 km from the shoreline). Likewise, an internet search resulted in digital photos showing pine pollen grains only in nearshore waters or on beaches. Given that the Baltic Sea is surrounded by countries rich in pine trees and other conifer plants, a natural question is whether pollen grains can also be found in other coastal waters or even open waters of the Baltic Sea, and, if so, where and when?

The objective of this work is to search for pollen grain aggregations in surface waters of the Baltic Sea using multi-sensor satellite imagery, and to document their spatial distributions and temporal changes. Through laboratory experiments and image analyses, we hope to answer the following questions:

- 1) What are the spectral characteristics of pine pollen grains that may be used for remote detection?
- 2) Where and when can pollen grains be found in the Baltic Sea, and is there a temporal trend?

2. Data and methods

2.1. Laboratory experiments

Laboratory experiments were used to measure spectral reflectance of pine pollen grains in the following ways.

First, pine pollen grains were collected by the Pomeranian University from male inflorescences directly from pine trees (*Pinus sylvestris*) of Northern Poland (4 km from shore of the Baltic Sea) in May 2018. In the laboratory, the pollen gains were carefully mixed with distilled water to obtain a suspension of pollen grains on the water surface. The concentration of pollen was high enough to cover the entire surface of the container, so the measured reflectance no longer changes with additional pollen. After 24 h, the pollen sample (including the container) was put outdoor under a cloud-free sky (Fig. 2a). The use of 24 h was to make pollen moist without decomposition. Reflectance was measured with a Satlantic Hyper Spectral Radiometer HyperPro (Fig. 2a) in 136 channels in the 350–800 nm spectral range. The HyperPro instrument was equipped with two hyperspectral sensors to measure downward irradiance ($E_d(\lambda)$, $W m^{-2} nm^{-1}$) and upward radiance ($L_u(\lambda)$, $W m^{-2} nm^{-1} sr^{-1}$), respectively. The measurements were repeated automatically every 2 s, with their averages being used to calculate the target (i.e., pollen) reflectance as $R = \pi L_u(\lambda) / E_d(\lambda)$. During the measurement, care was taken to avoid instrument self-shading so the instrument itself did not block the direct solar beam. Such measured reflectance were regarded to represent “pure” pollen that can be used as endmember spectra for spectroscopy analysis and for spectral unmixing, as shown below.

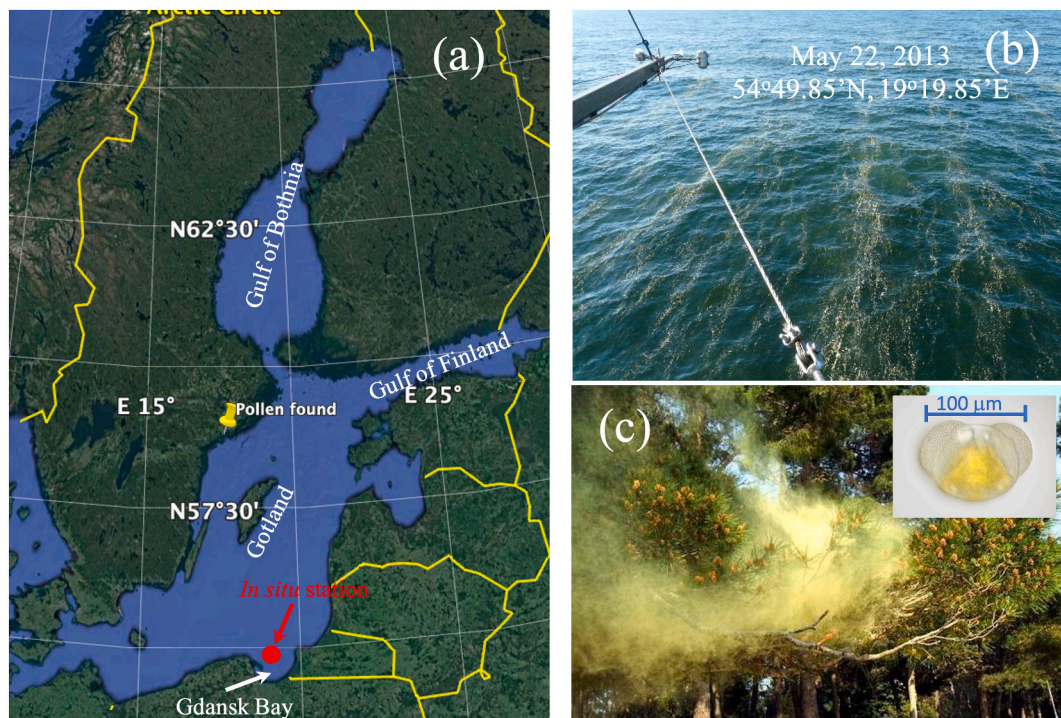


Fig. 1. (a) Google Earth map showing the Baltic Sea, with several subregions annotated. The pinned location is where pollen grains have been reported in Lienart et al. (2022), and the red dot shows the location where the digital photo in (b) was taken on 22 May 2013. More photos are presented in Fig. S1. (c) Pine pollination in Delaware Valley (online picture from <https://www.asthmacenter.com/pine-pollen-delaware-valley-may-2017/>). The inset photo shows a single pine pollen grain under microscope with a scale of about 50 μm (online picture source: <https://www.alamy.com>), resembling the shape of Mickey Mouse. (For interpretation of the references to color in this figure legend, the reader is referred to the web version of this article.)

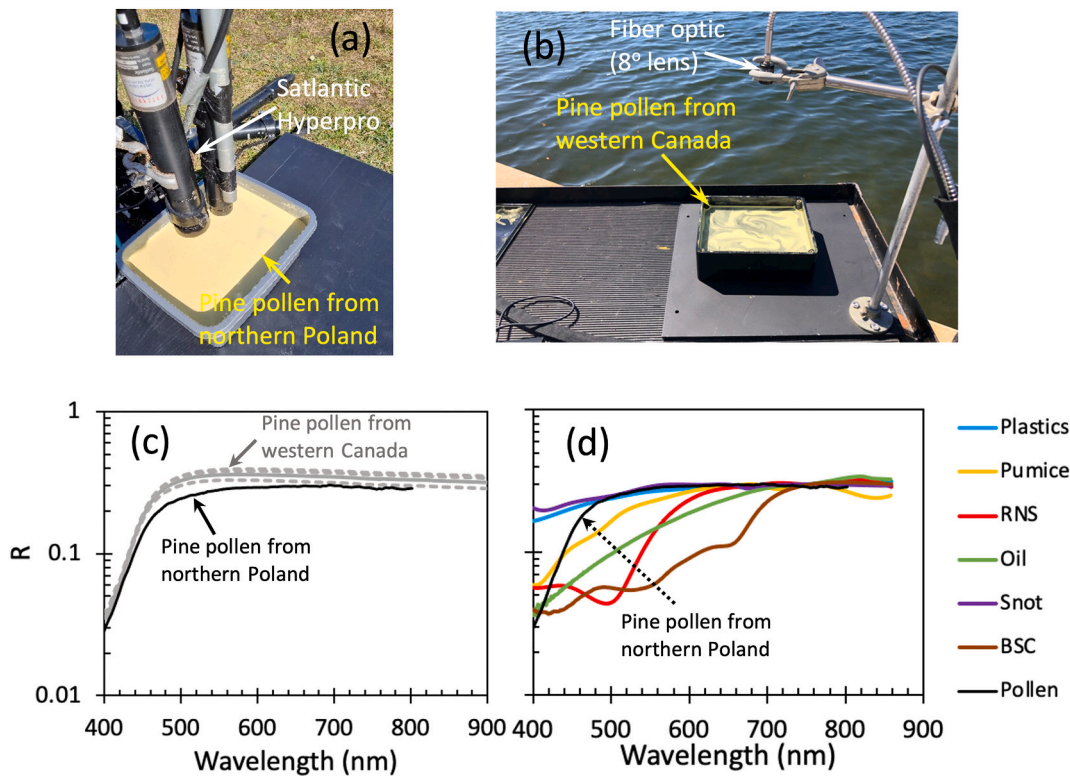


Fig. 2. (a) Outdoor experiments to measure reflectance of pollen on water on 4 June 2018, where pollen grains (*Pinus sylvestris*) were collected from male inflorescences directly from pine trees of Northern Poland (4 km from shore of the Baltic Sea) in May 2018; (b) Similar experiment on 17 March 2022, but pollen grains were harvested from Lodgepole Pine (*Pinus contorta*) trees from Western Canada; (c) Reflectance of pollen on water determined from the two experiments (each spectral curve is an average of multiple measurements). For both pollen species, there is a sharp increase from 400 to 500 nm, with the fastest changes between 400 and 460 nm; (d) Reflectance of various types of floating matters, obtained from the literature (Hu, 2021; Qi et al., 2019 & Qi et al., 2020; Lu et al., 2020; Hu et al., 2022), with pollen spectra overlaid. RNS: red *Noctiluca scintillans*; BSC: brine shrimp cysts. To facilitate visual comparison of spectral shapes, all spectra are plotted in log scale. The SAM values between the mean pollen spectra of (c) and individual pollen spectra are $<3^\circ$, but between the same mean pollen spectra of (c) and all other endmember spectra of (d) are $>10^\circ$ (plastics: 11.6° , pumice: 10.6° , RNS: 25.3° , oil: 19.5° , snot: 12.9° , BSC: 31.2°). (For interpretation of the references to color in this figure legend, the reader is referred to the web version of this article.)

Then, to determine whether different types of pine pollens have similar spectra, raw pine pollen grains were purchased by the University of South Florida from the Canadian Pine Pollen Company Ltd. in January 2022. These are raw, unpasteurized pollen grains that have been harvested from Lodgepole Pine (*Pinus contorta*) trees from the pristine forests of Western Canada. Unlike most commercial products, these pollen grains are unprocessed, i.e., the pollen cell walls are not cracked and therefore mimic the conditions in the natural environments. The pollen grains were carefully put on water in a black container overnight, from which reflectance was measured outdoor under a cloud-free sky (Fig. 2b). Reflectance was measured with a Spectral Revolution, Inc. SR1901 UV-VIS-NIR (Ultraviolet-Visible-Near infrared) spectrometer with an 8° FOV fiber optic lens and wavelength range of 325 nm – 1900 nm (1577 channels). A diffuse-white reflectance standard (an Avian Technologies Fluorilon-99 WTM with factory-provided reflectance values) placed in the same location as the black container was used as a reference. The ratio between the two measurements, after multiplying the reflectance of the reference standard, is the pollen grain reflectance (R): $R = R_r L/L_r$, where R_r is the reflectance of the reference standard provided by the manufacture, L is the measured radiance from pollen on water, and L_r is the measured radiance from the reference standard. Similar to the outdoor experiment in Poland, the USF experiment was also to determine the pollen reflectance spectra when the water is fully covered by pollen so the spectra could be used as endmember spectra to perform spectroscopy analysis and to perform spectral unmixing (see below). Therefore, as long as pollen grains fill the entire field of view of the fiber optic lens, the surface water area or the water volume does not impact the measurement because water is fully covered by pollen grains

and therefore does not contribute to the measured reflectance.

In both outdoor measurements, the pollen grains are floating on the very surface to imitate surface scums as observed from satellites. It is actually impossible to make the pollen grains suspended in water unless a wind blower is used to mix them into an unstable state – once the blower is stopped, the pollen grains start to float on the surface again.

2.2. Satellite image analyses and spectral diagnostics

While there are many satellite sensors that can detect the optical signals of pollen grains on the water surface, in this study those medium- and high-resolution sensors listed in Table 1 were used for varying purposes. The medium-resolution sensors include the Visible Infrared Imaging Radiometer Suite (VIIRS), the Moderate Resolution Imaging Spectroradiometers (MODIS), the Medium Resolution Imaging Spectrometer (MERIS), and the Ocean and Land Colour Instrument (OLCI). The high-resolution sensors are the MultiSpectral Instrument (MSI) on both Sentinel-2A and Sentinel-2B satellites.

Except for VIIRS, all medium-resolution data were obtained from the NASA's Ocean Biology Distributed Active Archive Center (OB.DAAC, <https://oceancolor.gsfc.nasa.gov>). All high-resolution data were obtained from the EUMETSAT Copernicus Open Access Hub. The low-level data were processed to generate Rayleigh-corrected reflectance ($R_{rc}(\lambda)$, dimensionless) using the SeaDAS software package (version 8.0) for the medium-resolution data, and using the Acolite software package (Github release in April 2021) for the high-resolution data. The use of $R_{rc}(\lambda)$ data instead of the fully atmospherically corrected remote sensing reflectance ($R_{rs}(\lambda)$, sr^{-1}) is because the enhanced near infrared (NIR) reflectance of

Table 1

Satellite sensors and their characteristics and usage in this study. For convenience, they are separated to medium-resolution and high-resolution sensors. SD: spectral diagnostics.

Sensor	Duration	Equatorial Revisit	Resolution	Data Products	Purpose	Data Source
Medium resolution						
VIIRS/SNPP	2011 – present	1 day	375–750 m	FRGB	Online browse	NOAA OCView
MODIS/T	2000 – present	1 day	250–1000 m	FRGB, R_{rc}	Time series	NASA OB.DAAC
MODIS/A	2002 – present	1 day	250–1000 m	FRGB, R_{rc}	Time series	NASA OB.DAAC
MERIS	2002–2012	3 days	300 m	FRGB, R_{rc}	SD	NASA OB.DAAC
OLCI/3A	2016 – present	3 days	300 m	FRGB, R_{rc}	SD	NASA OB.DAAC
OLCI/3B	2018 – present	3 days	300 m	FRGB, R_{rc}	SD	NASA OB.DAAC
High resolution						
MSI/2A	2015 – present	10 days	10–60 m	FRGB, R_{rc}	Detailed view + SD	EUMETSAT
MSI/2B	2017 – present	10 days	10–60 m	FRGB, R_{rc}	Detailed view + SD	EUMETSAT

the floating matters often led to erroneous $R_{rs}(\lambda)$ data due to atmospheric correction failure. The use of $R_{rc}(\lambda)$ data can avoid such problems through a reflectance differencing technique (Qi and Hu, 2021; Hu et al., 2022).

For visual inspection, the $R_{rc}(\lambda)$ data were mapped to an equidistant cylindrical projection, and then used to generate false-color Red-Green-Blue (FRGB) composite images (Qi et al., 2020). The spectral bands used in the FRGB images are 645 nm (red), 859 nm (green), and 469 nm (blue) for MODIS, and 671 nm (red), 862 nm (green), and 443 nm (blue) for VIIRS. The use of FRGB was to examine whether the NIR band had enhanced reflectance due to surface floating matters. Because pine pollination season around the Baltic Sea is between May and June, visual inspection was applied to images in May–July only from both VIIRS FRGB imagery through the NOAA OCView online portal (Mikelsons and Wang, 2018) and MODIS FRGB imagery generated for this project. Once a suspicious image feature was visually identified, its reflectance spectral shape from the same-day OLCI or MERIS image was examined and compared with pine pollen reflectance determined from laboratory measurements and with reflectance of other floating matters. Here, the use of OLCI or MERIS is because they have more spectral bands between 400 and 900 nm (with a nominal spatial resolution of 300 m) than other multi-band sensors, and therefore are more suitable for spectral diagnostics (e.g., Qi et al., 2020). Furthermore, MSI images corresponding to the image features found in medium-resolution images were also examined for their spectral shapes in a similar fashion as those with OLCI and MERIS. For MSI, because all spectral bands were first resampled to 10 m, a 5×5 pixel averaging was used to minimize the impact of mixed band resolutions on the spectral shapes (Hu, 2021, 2022).

The steps to examine spectral shapes of floating matters from satellite images have been outlined in Hu et al. (2022), where the subject is sea snout. The same principles and steps also apply to pollen grains in this study. Briefly, because reflectance of pollen grains with full pixel coverage is much higher than water reflectance for most visible and NIR wavelengths (see experimental results below) and because the subpixel coverage pollen grains can be very small (e.g., < 10% of a pixel), a spectral differencing technique was used to examine the spectral shape of pixels containing floating matter (in this case, pollen grains):

$$\begin{aligned}
 \Delta R_{rc}(\lambda) &= R_{rc}^T(\lambda) - R_{rc}^W(\lambda) \\
 &= (R^T(\lambda) + R_a(\lambda)) - (R^W(\lambda) + R_a(\lambda)) \\
 &= R^T(\lambda) - R^W(\lambda) \\
 &= [\chi R^{FM}(\lambda) + (1 - \chi)R^W(\lambda)] - R^W(\lambda) \\
 &= \chi(R^{FM}(\lambda) - R^W(\lambda)) \\
 &\approx \chi R^{FM}(\lambda) \text{ [assuming } R^W(\lambda) \ll R^{FM}(\lambda)\text{]}.
 \end{aligned}$$

Here, $\Delta R_{rc}(\lambda)$ is the difference between the target pixel (superscript “T”) and nearby water pixel (superscript “W”), χ (0.0%–100%) is the subpixel fraction of floating matter (FM), $R^{FM}(\lambda)$ is the floating matter surface reflectance at $\chi = 100\%$ (i.e., endmember reflectance), $R^W(\lambda)$ is the water surface reflectance from pixels nearby the floating matter. $R_a(\lambda)$ represents atmospheric reflectance due to aerosol scattering,

which is assumed to be the same between the target pixel and nearby water pixel. With $R^W(\lambda) \ll R^{FM}(\lambda)$, the spectral shape of $\Delta R_{rc}(\lambda)$ can be used to approximate $R^{FM}(\lambda)$, while their spectral magnitudes differ by an unknown factor of χ that can be estimated as

$$\chi = \Delta R_{rc}(\text{NIR}) / R^{FM}(\text{NIR}). \quad (2)$$

This is because the maximum reflectance contrast between floating matter and water is in the NIR wavelengths. $R^{FM}(\text{NIR})$ can be estimated from laboratory experiments, or determined from image pixels as the average of maximum $\Delta R_{rc}(\text{NIR})$ values. For sea snout, $R^{FM}(\text{NIR})$ was estimated to be 0.3. For pollen grains, the experimental results below also indicate that 0.3 is a reasonable assumption.

To determine whether the floating matter determined from the image analysis and spectral diagnostics is likely pollen grain, the spectral shape of $\Delta R_{rc}(\lambda)$ was compared with the spectral shape of pollen grains determined from laboratory experiments and with other floating matters that may also be found in marine or other water environments. The comparison was through both visual inspection and a spectral angle mapper index (SAM) (Kruse et al., 1993):

$$\text{SAM (degrees)} = \cos^{-1} \left[\left(\frac{\sum x_i y_i}{\left(\sqrt{\sum x_i^2} \sqrt{\sum y_i^2} \right)} \right) \right]. \quad (3)$$

Here, the subscript i is for band number, and x and y represent two spectral vectors from $\Delta R_{rc}(\lambda)$ of a pixel of interest and a spectral end-member determined from the experiment or obtained from the literature. From this definition, SAM depends only on the spectral shape as opposed to the spectral magnitude, with $\text{SAM} = 0^\circ$ for two identical spectral shapes and $\text{SAM} = 90^\circ$ for two completely different spectral shapes. For the former case, the two spectra would appear parallel to each other if plotted in logarithmic space.

2.3. Delineation of pollen rich water

From the above spectral diagnostics, once the image features were determined to contain pollen grains, the waters bounding these features were manually delineated. The method was applied to individual images where pollen features were found, and all water areas within a calendar year were combined to determine the approximate cumulative footprint of pollen-rich waters for that year. Ultimately, a method based on computer artificial intelligence may be developed to delineate such image features automatically and objectively (e.g., Qi et al., 2021), but the purpose here was to determine the boundary of water bodies encompassing the image features as opposed to the boundary of image features themselves. Therefore, simple manual delineation was deemed sufficient for this purpose and for the purpose of estimating the approximate cumulative footprint of pollen-rich waters. Furthermore, for a limited number of selected regions with clear sky conditions, a simple gradient method was used to delineate the image slicks whose pixels were determined (through spectral diagnostics) to contain pollen grains. For such image pixels, the subpixel coverage χ of each pollen-

containing pixel was estimated using Eq. (3), and their arithmetic average (including the pollen-free pixels) was used to represent the mean χ for the selected water regions. The “pure” pollen coverage (in km^2) was estimated to be a product of mean χ and the area of the pollen-rich waters.

3. Results

3.1. Pine pollen reflectance from outdoor experiments

Fig. 2c shows the reflectance from dense pine pollen grains in the experimental settings of Figs. 2a & 2b. From the multiple measurements of the two types of pollens, the reflectance shows near-identical spectral shapes, which can be characterized as: 1) lack of narrow-band features (i.e., no “sudden” changes in any wavelengths); 2) a sharp increase from ~ 400 to ~ 500 nm, after which the spectra become rather flat. In addition, reflectance between 700 and 800 nm is around 0.3.

Such characteristics are relatively unique among other floating matters that have also been reported in the aquatic environment, for example, macroplastics, sea snout, pumice rafts, brine shrimp cysts (BSCs), red *Nocticula scintillans* (RNS), and oil emulsions (Fig. 2d). Although these latter floating matters do not show any narrow-band features either, neither appears to show both characteristics identified above for pollen grains. Such a difference between pollen grains and other floating matters may be used to discriminate pollen grains from image features, as shown below. Note that reflectance spectra of many floating algae and other floating vegetation are not included in Fig. 2d because their common narrow-band feature around 670 nm (due to pigment absorption) makes them easily distinguishable from pollen reflectance.

3.2. Image and spectral features determined from multi-band imagery

Visual inspection of the VIIRS FRGB imagery through the NOAA OCView online portal showed extensive image slicks in many images between May and June of 2012–2021. While it is impossible to present

all images containing such slicks, Fig. 3 shows two examples in May 2018 and June 2021, respectively, where the image slicks are revealed clearly. Visual inspection of MODIS FRGB imagery showed similar features between May and June of 2000–2021 for most years. While the spatial shapes of these features can be well explained by sub-mesoscale dynamics (e.g., eddies of 0.1–10 km in size) (Onken et al., 2020; Chrysagi et al., 2021), what type of floating matters can result in such image slicks?

Corresponding to the two VIIRS images shown in Fig. 3, the OLCI images in Figs. 4a & 4b were used to analyze the spectral shapes of the image slicks, where ΔR_{rc} spectra from 100 randomly selected pixels of the image slicks from each of the two images are shown in the inset figures of Figs. 4a & 4b. To show more details, ΔR_{rc} spectra from three of such pixels (marked as “1”, “2”, “3” in Figs. 4a & 4b) are shown in Figs. 4c & 4d, respectively. Despite their differences in reflectance magnitudes (corresponding to subpixel coverage χ), their spectral shapes are nearly identical, indicating the same type of floating matter. The lack of spectral features suggests lack of pigments. Comparison between these $\Delta R_{rc}(\lambda)$ spectra and the $\Delta R_{rc}(\lambda)$ spectra of other floating matters (including pollen grains, see Figs. 2c & 2d) showed the lowest SAM values with pollen grains of the Baltic origin ($5.9 \pm 0.9^\circ$ for Fig. 4c, $6.6 \pm 2.6^\circ$ for Fig. 4d, see Table 2). Visually, the spectral shapes in Figs. 4c & 4d and in the inset figures all show sharp increases from the 412-nm to the 510-nm band, after which their reflectance appears rather flat. All these results suggest that the image slicks of Figs. 4a & 4b are likely due to pollen grain aggregations.

Even without the SAM analysis, knowledge of regional oceanography can also be used to rule out some other possibilities. For example, marine debris and sea snout can be both ruled out because the former could not reach such a large scale (for otherwise there would be extensive news coverage) and sea snout events typically last much longer (e.g., March – June 2021 in the Sea of Marmara, Hu et al., 2022). Therefore, considering that pine pollens are often found in the southern Baltic Sea (including the Gdansk Bay, Pawlik and Ficek, 2016, 2021, also see digital photos in Fig. S1), aggregation of pollen grains in surface waters is the most likely reason to explain the image slicks. This argument is

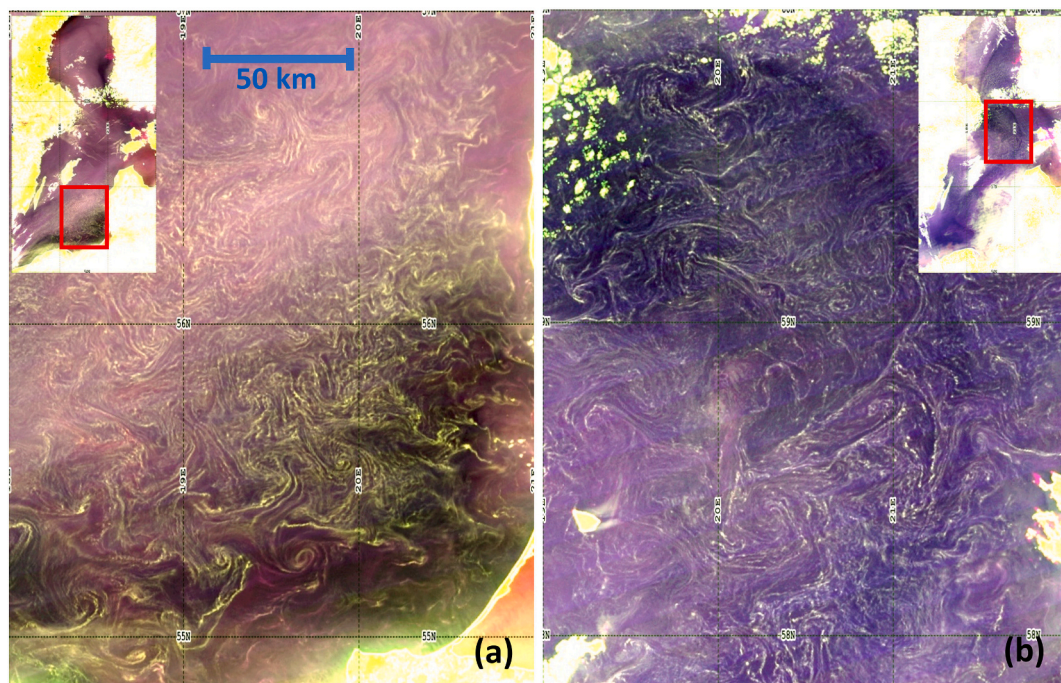


Fig. 3. VIIRS FRGB images on 16 May 2018 (a) and 5 June 2021 (b) showing surface slicks in the southern Baltic Sea (54.8357°N , $18\text{--}21^\circ\text{E}$) and northern Baltic Sea ($57.83\text{--}60^\circ\text{N}$, $19\text{--}22^\circ\text{E}$), respectively. The locations of the two regions are shown in the inset figures. The images were taken as screenshots from the NOAA OCView online portal, and then color stretched to highlight the surface features.

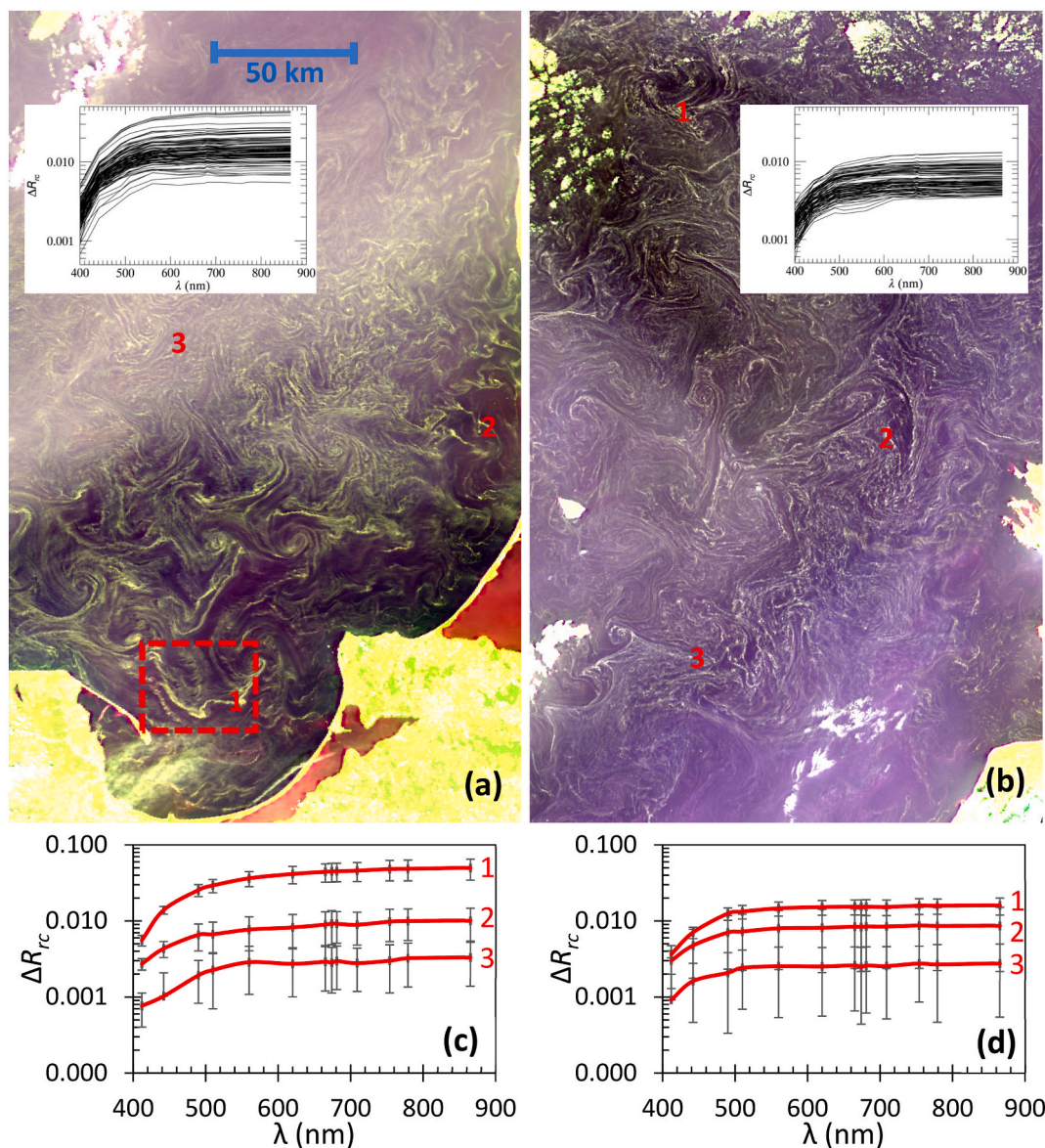


Fig. 4. OLCI/3A (a) and OLCI/3B (b) FRGB images on 16 May 2018 (08:51 GMT) and 5 June 2021 (09:19 GMT) showing surface slicks in the southern Baltic Sea (54.3–57°N, 18–21°E) and northern Baltic Sea (57.3–60°N, 19–22°E), respectively. These images correspond to those shown in Figs. 3a & 3b, respectively, but spectral shapes of 100 randomly selected pixels from the slick features are illustrated in the inset figures, and from three locations (marked as “1”, “2” “3”) are shown in (c) and (d), respectively. Solid lines and vertical bars represent mean and 1 standard deviation from 3×3 pixels, respectively. The dashed rectangular box in (a) shows the location of the MSI image, displayed in Fig. 5.

Table 2

SAM values between image features and floating matter endmembers. For OLCI, SAM was calculated using wavelengths of 412, 442, 490, 510, 560, 620, and 665 nm. For MSI, SAM was calculated using wavelengths of 443, 492, 560, 665 nm. Lower SAM values (bold font) indicate higher similarity. Here, “Plastics” refer to the macroplastic materials in Hu (2021), “BSCs” refers to brine shrimp cysts (Qi et al., 2020), and “RNS” refers to red *Noctiluca scintillans*. Note that the image features in the last row (OLCI image on 9 June 2020) represent cyanobacterial surface scums (Fig. 7).

Image features from	Floating matter endmember							
	Poland pollen	Canadian pollen	Sea snot	Plastics	Pumice raft	BSCs	RNS	Oil emulsion
OLCI, 5/16/2018, Fig. 4a, Baltic	5.9 ± 0.9	7.8 ± 1.0	13.8 ± 3.7	12.0 ± 3.7	6.3 ± 2.3	14.0 ± 1.4	24.6 ± 2.4	13.1 ± 2.6
OLCI, 6/5/2021, Fig. 4b, Baltic	6.6 ± 2.6	6.9 ± 2.4	9.7 ± 2.3	8.1 ± 2.3	10.7 ± 1.2	16.8 ± 0.5	29.2 ± 0.8	17.9 ± 1.1
OLCI, 6/6/2021, Fig. 8, Swedish lakes	3.5 ± 0.7	5.8 ± 0.9	15.3 ± 1.7	13.8 ± 1.7	6.8 ± 0.5	15.7 ± 0.4	25.4 ± 1.2	14.0 ± 0.9
MSI, 5/16/2018, Fig. 5, Baltic	4.1 ± 1.9	6.3 ± 2.4	14.1 ± 1.9	12.4 ± 1.8	7.7 ± 2.0	14.6 ± 1.7	23.7 ± 2.6	13.8 ± 2.5
MSI, 6/21/2018, Fig. 9, Temagami	5.1 ± 1.4	5.9 ± 2.3	16.1 ± 1.6	14.9 ± 1.6	10.9 ± 1.3	19.1 ± 1.2	26.6 ± 2.1	17.2 ± 1.9
OLCI, 6/9/2020, Fig. 7, Baltic	22.1 ± 1.3	22.6 ± 1.5	21.2 ± 4.4	21.8 ± 3.8	22.2 ± 1.7	29.4 ± 3.0	33.3 ± 3.1	27.3 ± 2.1

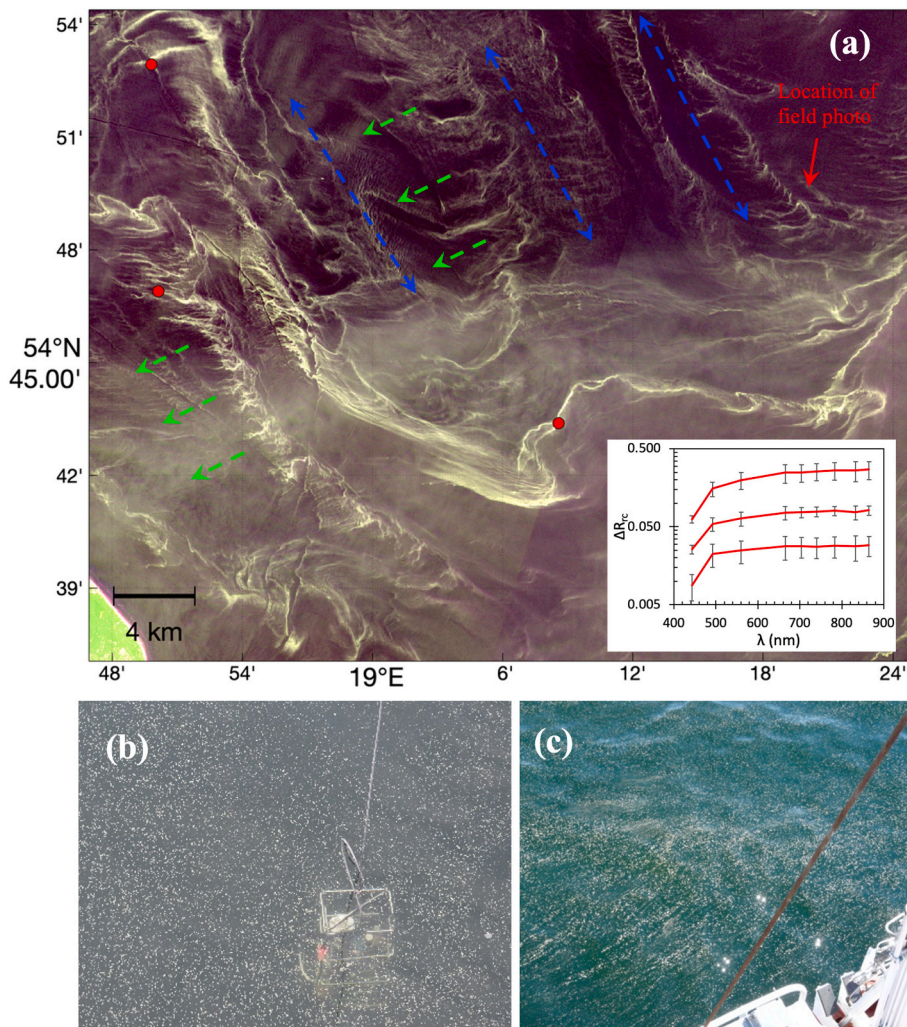


Fig. 5. (a) MSI FRGB on 16 May 2018 (10:00 GMT) showing surface slicks in the southern Baltic Sea (region outlined in red in Fig. 4a). The MSI image was collected on the same day as the OLCI image in Fig. 4a. The spectral shapes of randomly selected pixels (red dots) are shown in the inset figure, where solid lines and vertical bars represent mean and standard deviation from 5×5 10-m resolution pixels, respectively. The blue dashed lines indicate directions of major slicks, while the green dashed arrows indicate wind directions. The red arrow points to a location where a digital photo was taken on 15 May 2018, shown in (b). In this photo, pollen grains are visible to human eyes, and the optical profiling package has an approximate size of 0.5 m. Another photo in a nearby location was collected in May 2013, shown in (c). More digital photos are provided in Fig. S1. (For interpretation of the references to color in this figure legend, the reader is referred to the web version of this article.)

further reinforced by the more detailed view in Fig. 5 as well as other examples shown below.

Fig. 5a shows more detailed view of the same image features of Fig. 4a, but at a much higher resolution of 10 m. At this resolution, the spectral shapes of selected pixels show similar characteristics (inset figure of Fig. 5a) as their counterparts in the 300-m resolution OLCI image (Figs. 4a & 4c), but with more detailed slick structures revealed in the image. For example, along the major slicks found in the 300-m resolution OLCI image (Fig. 4a), there are smaller feather-like features, often parallel to each other in the NEE-SWW direction that appear to be the result of wind-driven Langmuir circulation (Fig. 5a). While the orientations of the major slicks are believed to be dominated by surface currents (NW – SE direction in the case of Fig. 5a), the directions of smaller features along the major slicks are likely driven by the easterly and northeasterly winds (Fig. S2). For this MSI image, digital photos collected from a ship just one day earlier (Fig. 5b & 5c, note the optical profiling package in the photo) provided a direct confirmation of pollen grains on the water surface in the location pointed by the red arrow in Fig. 5a. More digital photos are provided in Fig. S1 to show the appearance of pollen in water.

3.3. Pollen water footprint in the Baltic Sea

While OLCI provides spectral diagnostics of the image features at 300-m resolution, more images are available from MODIS observations. Inspection of the MODIS FRGB images of 2000–2021 showed the same

image features as in Figs. 3 & 4, whose spectral shapes from the corresponding MERIS or OLCI images were all similar to those shown in Figs. 4c & 4d. Therefore, these image features can be inferred to be caused by pollen grain aggregations. For illustration purpose, several additional examples are provided in the supplemental figures (Figs. S3 – S6). These examples clearly show that pollen aggregations can be found nearly everywhere in the Baltic Sea. Although the starting and ending days when pollen aggregations were observed in an individual year varied due to availability of cloud free images, during the 22-year period, the earliest day showing pollen aggregations is May 10 (in 2000) and the latest day is June 16 (in 2006). In 2018, pollen aggregations were found between May 12 and June 2, a period of 22 days (the longest duration identified in this time series).

The use of MODIS also showed approximate pollen distributions starting from 2000, defined as the cumulative footprint of pollen-rich waters (Fig. 6). Although these are only crude estimates from the simple delineation, they do show interesting spatial patterns in individual years and changes across different years as well as an apparent increasing trend. For example, during the first half of this period (2000–2010), pollen aggregations were found in 7 years, but mostly in relatively small regions (e.g., around Gotland island) except during 2010 when pollen aggregations were found along the east coast of the Baltic Sea. During the second half of this period (2011–2021), pollen aggregations were also found in 7 years, but in most of these years their footprints are much larger than those during the first half, especially in the later years of 2018 and 2021 when most of the Baltic Sea waters were

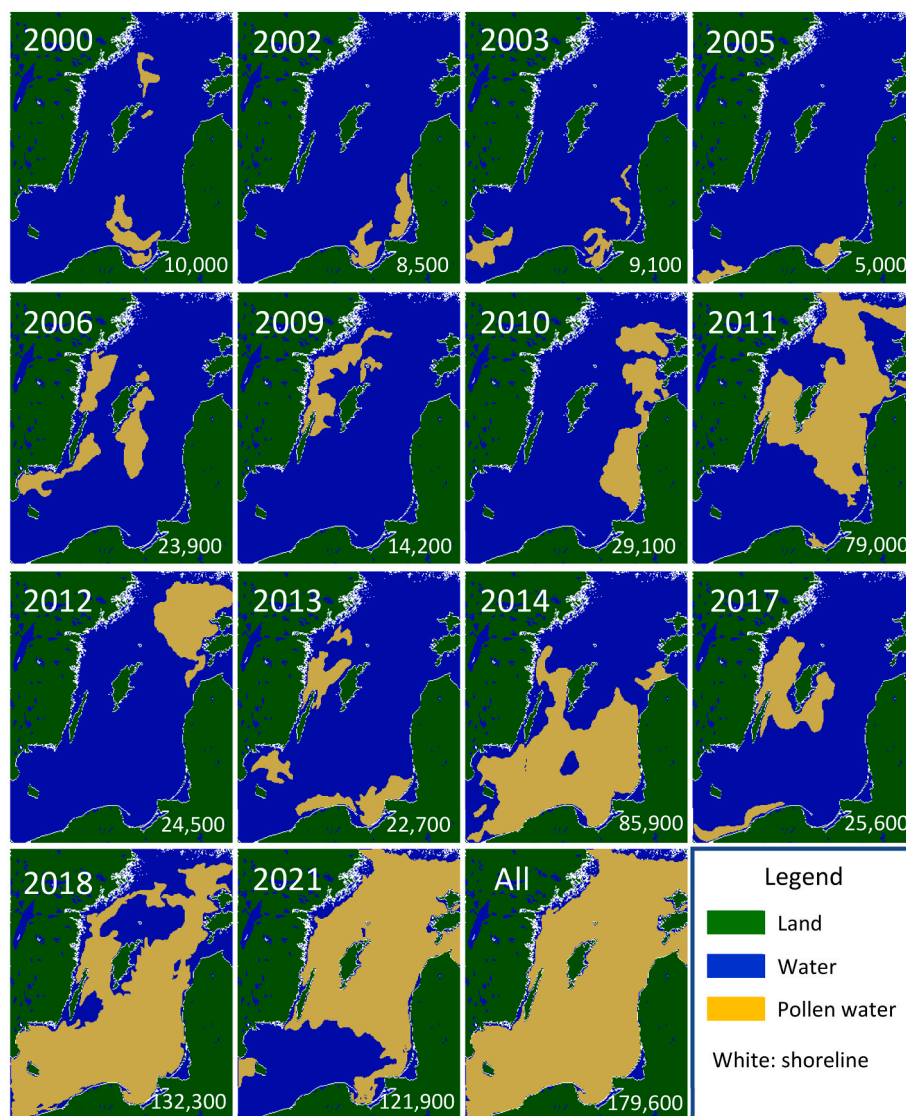


Fig. 6. Cumulative footprint of waters where surface slicks of pollen grains were found from MODIS observations. These maps cover a region of 54–60°N, 14–23°E. The water area (in km²) rich in pollen is annotated on the bottom right corner of each panel. The last panel represents all years combined.

found to contain pollen grains. In all years combined, the cumulative footprint shows that pollen aggregations can be found nearly everywhere in the Baltic Sea (Fig. 6 last panel).

4. Discussion

4.1. Is it really pollen?

As shown in Figs. 2b&2c, although there are some common characteristics between pollen and other non-algae floating matters in their spectral shapes (e.g., lack of narrow-band features, near monotonic increase from the blue to the red wavelengths), the sharp increase from ~400 nm to ~500 nm appears to be a unique feature in pollen reflectance, thus can be used for spectral discrimination. Indeed, the SAM-based analysis indicates lower SAM values between the image features and pollen grains than those between the image features and other floating matters (Table 2), suggesting the possibility of pollen grains. The limited field surveys also confirmed the presence of large amount of pollen grains on the water surface (digital photos of Fig. 5b & 5c, and digital photos in Fig. S1). Sea snout and marine debris can be easily ruled out also because they do not occur at this extensive scale in such a short period. Then, for the Baltic Sea, without the spectral diagnostics, the

only other possible floating matter is the annually occurring cyanobacterial blooms (Kahru et al., 2016, 2020), which are known to form patchy surface scums in the Baltic Sea (Reinart and Kutser, 2006). Fig. 7 shows one such case, where surface slicks are found in the OLCI FRGB image. However, the image slicks have a greenish color due to the red-edge reflectance, and the $\Delta R_{rc}(\lambda)$ spectral shapes from several randomly selected slicks (annotated as “1”, “2”, “3”) show a typical absorption feature around 670 nm, a red-edge reflectance in the NIR, and a local reflectance peak in the green wavelength (Fig. 7). These are dramatically different from the spectral shapes of pollen grain aggregations, but they show typical spectral shapes of cyanobacterial scums in the Baltic Sea (Reinart and Kutser, 2006). The SAM values between these image features and pollen endmember spectra are about 22° (Table 2 last row). Thus, the use of spectral diagnostics can rule out the possibility of cyanobacterial surface scums. Note that although cyanobacterial blooms in the Baltic Sea generally occur in the summer while pollen aggregations are mostly found in late spring, there appears to be an overlapping time window to make it difficult to make inference using imaging time alone. For the case shown in Fig. 7, the image was collected on June 9, within the time window of images with pollen features (May 10 (of 2000) – June 16 (of 2006)).

Other than the spectroscopy-based arguments, several other reasons

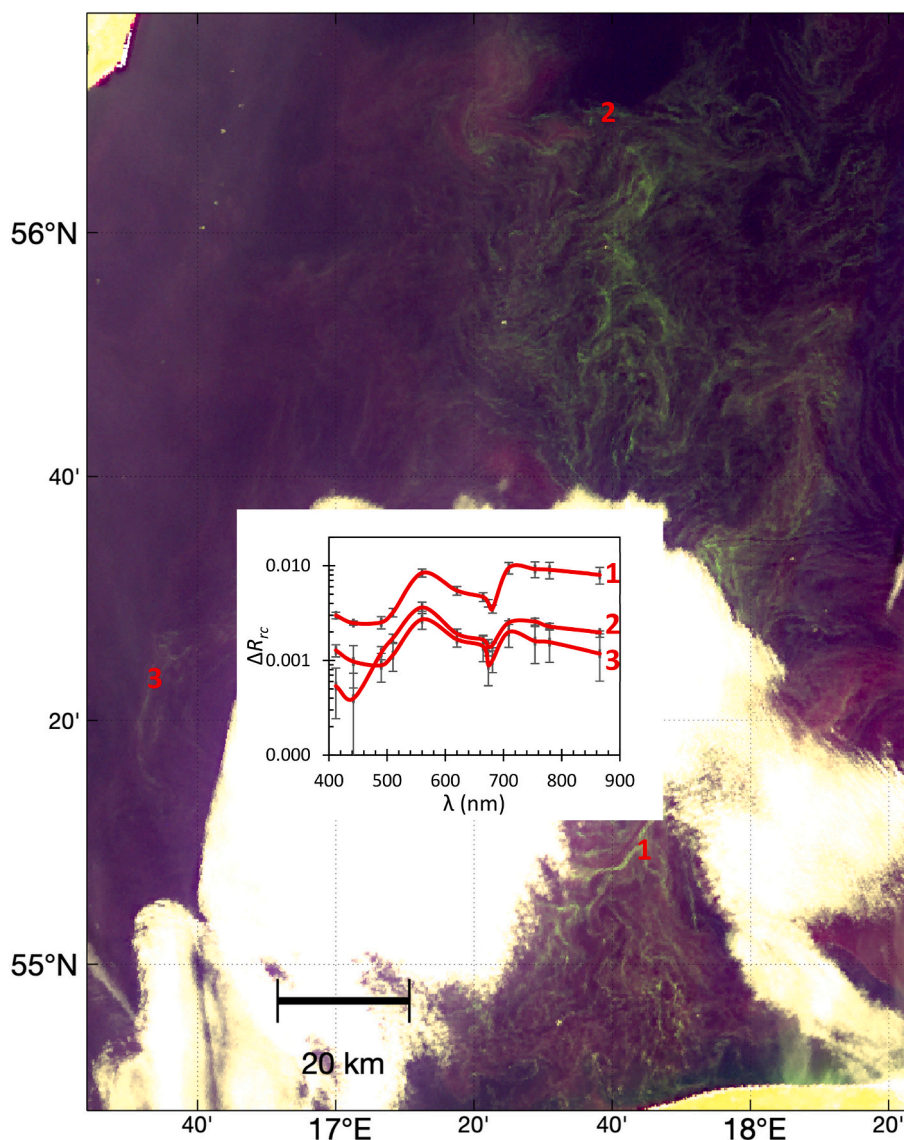


Fig. 7. OLCI FRGB image on 9 June 2020 (09:17 GMT) showing surface slicks in the southern Baltic Sea. The spectral shapes of several randomly selected image slicks (annotated as “1”, “2”, “3”, inset figure) indicate cyanobacterial surface scums instead of pollen grains. The SAM values between these features and pollen endmember spectra as listed in [Table 2](#) (last row).

also suggest that the image slicks in [Figs. 3-5](#) and [Figs. S3-S6](#) are due to pollen aggregations.

First, pollen aggregations have been reported in the month of May in both southern Baltic Sea (around Gdansk Bay of Poland, [Pawlik and Ficek, 2016, 2021](#)) and western Baltic Sea (near Stockholm University of Sweden, [Lienart et al., 2022](#)) ([Fig. 1](#)). It is a logical inference that pollen grains may be found in other regions of the Baltic Sea in the same month, as shown here. In fact, sediment samples from several sediment coring sites of the Baltic Sea all indicate pollen deposits, with pine pollen dominating the pollen counts ([Miettinen et al., 2002](#); [Van Wirdum et al., 2019](#)). The results here suggest that pollen grains are not limited to those sites, but can be found in sediment samples nearly everywhere in the Baltic Sea.

Then, if this is the case, similar pollen grain aggregations should also occur in nearby lakes and other waters in the same months as they are also surrounded by pine trees (mostly *Pinus sylvestris*). For example, the Gulf of Bothnia (60–65.9°N, ~45,174 mile²) and the Gulf of Finland (23–30.2°E, 11,583 mile²) are the northernmost and easternmost arms of the Baltic Sea, respectively ([Fig. 1](#)). Although not shown in this paper for brevity, VIIRS images on 8 and 9 June 2021 showed surface slicks up

to 65°N in the Gulf of Bothnia ([Fig. S7](#)) and up to 28°E in the Gulf of Finland ([Fig. S8](#)), which were confirmed to have the same $\Delta R_{rc}(\lambda)$ spectral shapes as those from pollen aggregations. Likewise, the two largest lakes in Sweden (west of the Baltic Sea), Lake Vänern and Lake Vättern, were also found to show image slicks that appear like pollen aggregations ([Fig. 8](#), [Table 2](#)).

Lastly, using the same logic, lakes in other regions that are surrounded by pine trees should also show similar slicks in satellite imagery during the pollination months. A search of satellite images confirmed this speculation, with an example shown in [Fig. 9](#) for Lake Temagami of Canada. Not only do the image slicks of [Fig. 9a](#) have similar spectral shapes as those of pollen aggregations ([Fig. 9b](#)), but digital photos taken from the lake on the same day as well as the online report showing these digital photos confirmed the presence of pollen aggregations ([Fig. 9c](#)).

Thus, all these arguments and evidence suggest that the image slicks cannot be due to other reasons than pine pollen aggregations.

4.2. Requirements on spectral and spatial resolutions

Although pollen has spectral shapes dramatically different from all

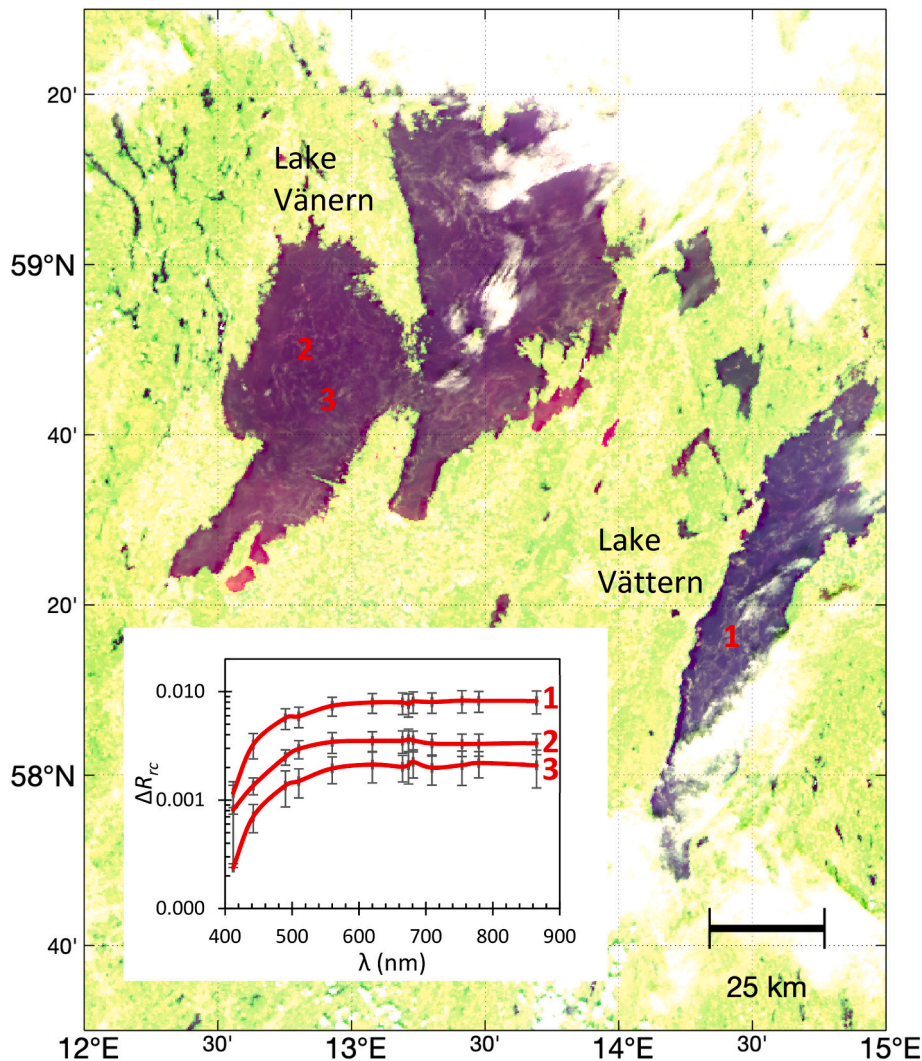


Fig. 8. OLCI FRGB image on 6 June 2021 (09:32 GMT) showing surface slicks in Lake Vänern and Lake Vättern (Sweden), respectively, where the spectral shapes of randomly selected image slicks (annotated as “1”, “2”, “3”) indicate possible pollen aggregation on the surface (inset figure). The SAM values between these features and pollen endmember spectra are listed in Table 2.

other known floating matters, most of these reflectance spectra show general increasing patterns from the blue to the red without narrow-band features (Figs. 2c & 2d), thus raising the question of what spectral resolution is required to discern their differences. From the spectral comparison, most of the difference between pollen and other floating matters occurs between 400 and 500 nm. Therefore, as long as there are two spectral bands from 400 nm to 500 nm (to show the sharp increase) and two more spectral bands beyond 500 nm (to show the plateaued reflectance shape), the spectral resolution should be sufficient to discriminate pollen aggregations from other floating matters. This is why all sensors used in this study are adequate for spectral discrimination, and this is also explained in Table 2 caption where only 4 MSI bands were used in calculating the SAM values.

Similar to spectral resolution, sufficient spatial resolution is required to detect the small pollen aggregations on the water surface (e.g., Fig. S1), which are often smaller than a pixel size. In this case, full pixel coverage is not required for either detection of presence/absence or spectral discrimination of pollen against other floating matters. Assuming that pixels with full coverage ($\chi = 100\%$) of floating matter have reflectance of ~ 0.3 in the NIR, the lower detection limit and discrimination limit, in terms of χ , depend only on the sensor's signal-to-noise ratios (SNRs) that determine the noise-equivalent reflectance measured under typical ocean conditions (Qi and Hu, 2021). The

physical detection limits, in terms of meters, are simply products of χ and the pixel size. Based on the analysis of SNRs and noise propagation, Qi and Hu (2021) determined that the spectral differencing technique used here can detect the presence of floating matters down to 2% of the MSI pixel size, and can discriminate floating matter type down to 6% of the MSI pixel size even in very turbid waters. This is because, regardless of the magnitude of χ (see Eq. 1), the spectral shapes of the image features in Figs. 5 & 9 are nearly identical to those of pollen aggregations (Table 2), and in spectral discrimination the shape indicates the type of floating matter while the magnitude indicates the magnitude of χ (Eq. 1). In Fig. 5, the NIR reflectance of the 3rd curve is about 0.03, suggesting $\chi \sim 10\%$ (assuming 0.3 corresponds to $\chi = 100\%$, see Fig. 2c). In Fig. 9b, the NIR reflectance of the third curve is about 0.004, suggesting $\chi \sim 1.3\%$. This means that in the 10-m resolution MSI images, elongated image slicks of pollen grains can be detected and discriminated without ambiguity as long as the equivalent slick width in the field is $> 1.3\% \times 10 \text{ m} = 13 \text{ cm}$.

This principle has been used to detect and discriminate *Sargassum* and *Ulva* (Fig. 7 of Qi and Hu, 2021), sea snail (Fig. 3 of Hu et al., 2022), and driftwood (Fig. 7a of Hu, 2022) without ambiguity even though these floating matters are only a few percent of a pixel size.

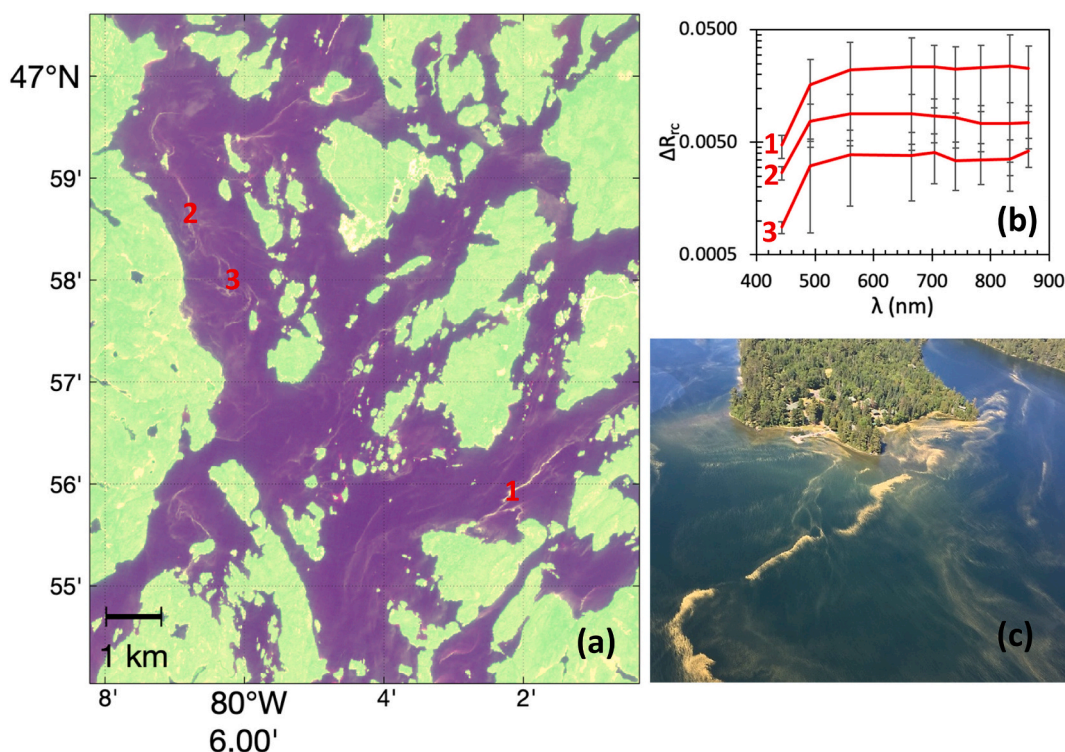


Fig. 9. (a) MSI FRGB image on 21 June 2018 showing surface slicks in Lake Temagami, Canada, where the spectral shapes of randomly selected image slicks (annotated as “1”, “2”, “3”) indicate possible pollen aggregation on the water surface (b). The SAM values between these features and pollen endmember spectra are listed in Table 2. (c) Digital photo taken from Lake Temagami on 21 June 2018 showing pine pollen on the surface (photo credit: Ron Miller of <http://Ottertooth.com>). More photos and descriptions of the annual pollen events in this lake can be found at <http://www.ottertooth.com/Temagami/Seasons/summer/2017summer-01.htm>.

4.3. Implications for ecology and carbon sequestration

The importance of pine pollen as a carbon source to invertebrates and as a terrestrial particle source to influence optical properties of the Baltic Sea have been demonstrated through case studies (Pawlik and Ficek, 2016, 2021; Lienart et al., 2022). Of the 22 years examined, 14 years showed pollen grains in surface waters of the Baltic Sea. Because the number of cloud-free images during the pollination season is similar in every year, it is unclear why pollen grains were missing in certain years. Without further investigations, we can only speculate that winds and precipitation conditions in those years were not favorable for long-distance transport of these fine particles. Nevertheless, in 2018 and 2021, pollen grains were found in nearly the entire Baltic Sea. The temporal trend shown in Fig. 6, although qualitative by its nature, suggests that its importance may have increased in the past decade for the Baltic Sea and, after logical extension, possibly for global water bodies under similar pollen influence. Indeed, the increased pollen coverage is in line with several earlier studies which showed more pollen production under higher CO_2 concentration and higher temperature (Ziska and Caulfield, 2000; Albertine et al., 2014), with pollination season becoming earlier and longer in North America and increases in tree pollens being more prominent than in grass or weed pollen (Anderegg et al., 2021). The increased pollen coverage is also in line with Kahru et al. (2016), where more surface incoming shortwave irradiance and warmer waters were found in recent years than in the 1980s. On the other hand, while pine pollen powder has been used widely as a nutrition source for humans and they are more ubiquitous than previously thought, their impacts on ocean (and lake) ecology, bio-optical properties, primary production, and carbon cycling are all understudied.

Such a lack of study hinders direct comparison between pollen and phytoplankton on their contribution to carbon sequestration.

Nevertheless, with some assumptions and simple calculations, a first-order comparison is provided below to present a context for pollen as a terrestrial carbon source.

Assuming $\Delta R_{rc}(859) = 0.3$ for “pure” pollen within a pixel (i.e., endmember reflectance), the pollen density on the water surface within several small regions of the MODIS image on 7 June 2021 was estimated to be ~ 0.001 (or 0.1%). Ideally, such estimates should be derived from all image features of every image. However, because of the lack of an algorithm to extract these features automatically, 0.1% was assumed to represent the typical pollen density in pollen rich waters. Then, assuming 0.2 kg m^{-2} density of pollen grains when the surface is fully covered by pollen, such a mean density of 0.1% corresponds to 0.2 g m^{-2} . The total amount of pollen corresponding to the 2018 case ($130,000 \text{ km}^2$) is calculated as: $M_{\text{pollen}} = 130,000 \times 10^6 \times 0.2 \times 0.001 = 26,000$ tons of pollen. According to an online report (<https://www.snopes.com/fact-check/pollen-cloud-tree/>), a pollen tree “can produce up to 5 lbs. (2.2 kilograms) of pollen in just a few weeks.” Assuming 1 kg per tree and 500 trees per acre, it would require only $\sim 210 \text{ km}^2$ pine forest, a tiny portion of all pine forests around the Baltic Sea, to produce 26,000 tons of pollen.

For this much pollen on water, assuming 49.5% carbon content (Rösel et al., 2012), the mean pollen carbon density in pollen-rich waters is $0.2 \times 49.5\% = 0.099 \text{ g m}^{-2}$, with the total amount of pollen carbon estimated to be 12,870 tons. Note that unlike recycled carbon within the water column, the pollen carbon represents “new carbon” to the Baltic Sea. The question is, is this new carbon significant compared to carbon sequestration by phytoplankton? With a mean net primary production (NPP) of $3 \text{ g carbon day}^{-1} \text{ m}^{-2}$ (based on MODIS estimates using a community accepted model, Behrenfeld and Falkowski, 1997) and assuming 0.3% of this amount can reach the sea floor and be permanently buried (Muller-Karger et al., 2005), carbon sequestration of phytoplankton is about $0.009 \text{ g day}^{-1} \text{ m}^{-2}$. Assuming 80% of pollen

particles are eventually buried on the sea floor and the estimated pollen amount represents the entire pollination season, the buried pollen is 0.079 g m^{-2} , corresponding to 9 days of phytoplankton carbon sequestration. If multiple pollen deposition events occur in one season with each contributing similar amounts, the buried pollen may be equivalent to 10–20 days of phytoplankton carbon sequestration. We acknowledge that due to the many assumptions used here, such estimates are subject to large uncertainties. For example, there is no information on the proportion of pollen particles that are eventually buried before they are consumed by bacteria or invertebrates, which also points to the need of more field-based studies. Nevertheless, these estimates are expected to serve as a first order reference in the context of carbon sequestration.

The estimations of pollen amount were based only on the observed pollen-on-water features. If sub-surface pollen grains are included, the estimates will be higher. For example, Fig. 10 shows that, among the surface slicks of pollen grain aggregations in the southwest Baltic Sea, there are subtle slick features that show different color shades (in this case, pinkish color). Comparison between the spectral shapes of these subtle features and the nearby surface slicks (inset figure of Fig. 10) shows a monotonic reflectance decrease from the green to the NIR bands in the former, indicating the same type of floating matter but that the floating matter is submersed in water. This is because the monotonic increase in light attenuation can cause monotonic decrease in reflectance. Assuming the light attenuation is dominated by water molecules in the NIR wavelengths, the submersed depth in this case was estimated to be $\sim 0.2 \text{ m}$. Inspection of other images showed similar image features that appear to be submersed pollen grain aggregations, but they were discarded in the pollen estimates, suggesting that the pollen estimates are conservative and further reinforcing the role of pollens in carbon sequestration and ecology. On the other hand, these subsurface features also suggest more work in developing improved algorithms to detect and

quantify them.

4.4. Other implications

As a proof-of-concept, this is the first study to demonstrate that pollen on water can be detected and possibly quantified from space. Much remains to be done, however. For example, an immediate follow-on work may be developing robust algorithms to quantify pollen density on the water surface and pollen concentration in the water column, which requires targeted field work in the near future. Likewise, it is currently unknown what caused the widespread pollen in the entire Baltic Sea: terrestrial discharge, atmospheric deposition (e.g., Sugita, 1993; Bunting and Middleton, 2005), or both. In this regard, targeted models may be developed to explain the widespread patterns.

Before such algorithms or models are developed and validated, the slick patterns revealed in the satellite images may be used to study submesoscale ocean dynamics. Previously, such dynamics are usually studied with numerical simulations (Onken et al., 2020; Chrysagi et al., 2021) due to lack of observing techniques. The spatial patterns of the image slicks (Figs. 3 & 4) can be well explained by the submesoscale dynamics and, in turn, may be used to validate numerical models in their estimated frontal density, among other parameters.

The findings of this study are also relevant to satellite ocean color vicarious calibration and product validation (Zibordi et al., 2009; Mélin and Zibordi, 2010). Because vicarious calibration requires spatially homogeneous waters around the calibration site, the presence of pollen grains may violate this assumption. Likewise, validation of ocean color data products often uses 3×3 image pixels to compare with a point measurement in the field, with implicit assumption of homogeneous waters within the pixels. The patchy aggregations of pollen grains may bring additional uncertainties in such validations. Therefore, interpretation of both field and satellite data during the pollination season requires extra caution.

Last but not least, the spectral shapes of pollen on water and the findings of this study have significant implications on remote detection of marine litter (i.e., marine debris, including plastics). Similar to sea snout (Hu et al., 2022), pollen aggregations on the water surface may present another confusion factor for remote detection of marine debris. This is because they all have similar spectral shapes of featureless reflectance that increases from the blue to the green and red wavelengths. Although the sharp increases from 400 nm to 500 nm only appear in pollen reflectance from laboratory measurements (Figs. 2c & 2d), due to light attenuations and other effects, such sharp increases may be compromised in satellite-derived spectra (Figs. 4c & 4d), making it difficult to differentiate pollen grains from marine debris using spectroscopy alone. For example, for the image slicks of Fig. 4b, although their SAM values with pollen grains ($6.6 \pm 2.6^\circ$) are lower than those with macroplastics ($8.1 \pm 2.3^\circ$), statistically their difference is not significant. In such cases, ancillary information such as the occurrence time, location, scale, and duration may be used to make educated inference. As such, in the case of the Baltic Sea, pollen aggregations were not found outside the time window of May 10 – June 16. In the case of sea snout events in the Marmara Sea, sea snout features were not found from satellite imagery outside the time window of late spring – early summer. Nevertheless, pollen on water represents another factor to consider when remote detection of marine debris is attempted.

5. Conclusion

This is perhaps the first report that shows extensive distributions of pollen grains in any marginal seas. A key finding is that, in certain years between May 10 and June 16, pine (*Pinus sylvestris*) pollen grains can be found in surface waters nearly everywhere in the Baltic Sea, well beyond nearshore or coastal waters. Such a discovery is attributed to the frequent multi-spectral satellite observations and the relatively unique reflectance spectral shapes of pine pollen grains, which are confirmed by

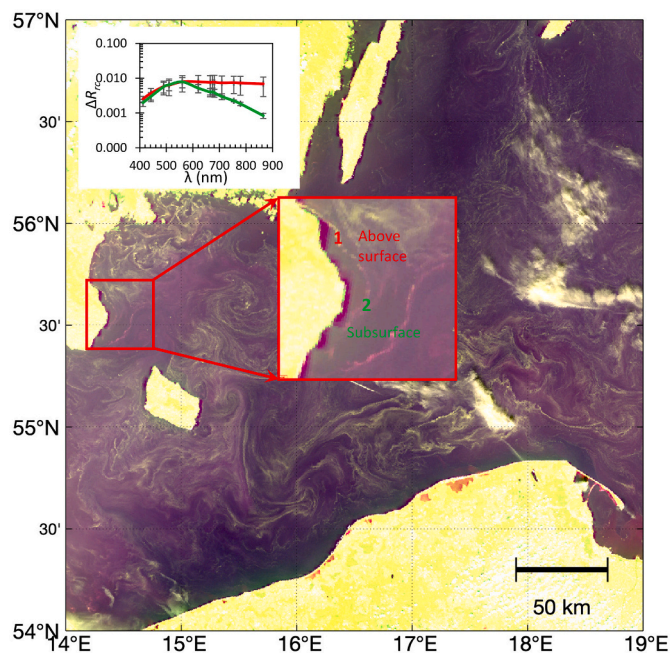


Fig. 10. OLCI FRGB image on 23 May 2018 (09:10 GMT) showing surface slicks in the southwest of the Baltic Sea (54–57°N, 14–19°E). The spectral shapes of the slicks appear like pollen grains. The inset figure shows two spectra from image slicks that appear to be on the surface and below surface (red and green in the inset zoom-in image), respectively. All satellite-based observations in this study were based on the former cases (i.e., surface scums of pollen grains), although the latter subsurface cases were also occasionally observed. (For interpretation of the references to color in this figure legend, the reader is referred to the web version of this article.)

laboratory experiments. Given the potential importance of pine pollen grains in carbon sequestration and other science, further studies are required to fully understand their corresponding roles. On the other hand, pollen grains can add additional difficulty in remote sensing of marine debris during the pollination season.

Notations

R	Reflectance (dimensionless)
R_{rc}	Reflectance after Rayleigh Correction (dimensionless)
R_w	Reflectance of pollen-free water, often derived from pixels near the pollen slicks
ΔR	Reflectance difference between pollen-containing and pollen-free water pixels (dimensionless)
χ	Subpixel pollen coverage (%), also called areal density
MERIS	Medium Resolution Imaging Spectrometer (2002–2012)
OLCI	Ocean and Land Color Instrument (2016 – present on Sentinel-3A, 2018 – present on Sentinel-3B)
VIIRS	Visible Infrared Imaging Radiometer Suite (2011 – present on SNPP)
MODIS	Moderate Resolution Imaging Spectroradiometer (2000 – present on Terra, 2002 – present on Aqua)
MSI	MultiSpectral Instrument (2015 – present on Sentinel-2A, 2018 – present on Sentinel-2B).
SAM	Spectral Angle Mapper ($0^\circ - 90^\circ$), an index to measure the similarity of spectral shapes between two reflectance vectors. SAM = 0° indicates identical spectral shapes, while SAM = 90° indicates completely different spectral shapes
NIR	Near infrared
SWIR	Shortwave infrared
FRGB	False-color Red-Green-Blue, where an NIR band is used in the green channel.
OCView	Ocean Color Viewer, an online image visualization tool developed by the U.S. NOAA (https://www.star.nesdis.noaa.gov/socd/mecb/color/ocview/ocview.html)

Credit author statement

Chuanmin Hu: Conceptualization; Funding acquisition; Methodology; Data Curation; Writing – original draft preparation, editing, revising.

Lin Qi: Conceptualization; Methodology; Data curation; Writing – original draft preparation, editing, revising.

David English: Methodology; Data curation; Writing – editing, revising.

Menghua Wang: Supervision; Funding acquisition; Writing – editing, revising.

Karlis Mikelsons: Data curation; Writing – editing, revising.

Brian Barnes: Data curation; Writing – editing, revising.

Magdalena Pawlik: Data curation; Funding acquisition; Writing – editing, revising.

Dariusz Ficek: Data curation; Writing – editing.

Declaration of Competing Interest

The authors declare that they have no known competing financial interests or personal relationships that could have appeared to influence the work reported in this paper.

Data availability

All data and images are available from NASA OB.DAAC (<https://oceancolor.gsfc.nasa.gov>), EUMETSAT Copernicus Open Access Hub (<https://scihub.copernicus.eu/dhus/#/home>), and NOAA OCView online portal (<https://www.star.nesdis.noaa.gov/socd/mecb/color/ocview/ocview.html>).

Acknowledgements

This work was supported by the U.S. NASA (80NSSC20M0264, 80NSSC21K0422), the Joint Polar Satellite System (JPSS) funding for the NOAA ocean color calibration and validation (Cal/Val) project, and by the National Science Centre of Poland (contract No. 2017/25/N/ST10/02578 to M.M.P). We thank NASA, NOAA, and EUMETSAT for providing all satellite data in this work. We are grateful to the anonymous reviewers, and in particular to Dr. Frédéric Mélin for their valuable comments and suggestions. The scientific results and conclusions, as well as any views or opinions expressed herein, are those of the author(s) and do not necessarily reflect those of NOAA or the Department of Commerce.

Appendix A. Supplementary data

Supplementary data to this article can be found online at <https://doi.org/10.1016/j.rse.2022.113337>.

References

- Albertine, J.M., Manning, W.J., DaCosta, M., et al., 2014. Projected carbon dioxide to increase grass pollen and allergen exposure despite higher ozone levels. *PLoS One* 9 (11), e111712. <https://doi.org/10.1371/journal.pone.0111712>.
- Anderegg, W., et al., 2021. Anthropogenic climate change is worsening North American pollen seasons. *PNAS* 118 (7), e2013284118. <https://doi.org/10.1073/pnas.2013284118>.
- Antoine, D., Babin, M., Berthon, J., Bricaud, A., Gentili, B., et al., 2014. Shedding light on the sea: Andre Morel's legacy to optical oceanography. *Annu. Rev. Mar. Sci.* 6, 1–21. <https://doi.org/10.1146/annurev-marine-010213-135135>.
- Behrenfeld, M.J., Falkowski, P.G., 1997. Photosynthetic rates derived from satellite-based chlorophyll concentration. *Limnol. Oceanogr.* 42, 1–20.
- Berthon, J.-F., Zibordi, G., 2010. Optically black waters in the northern Baltic Sea. *Geophys. Res. Lett.* 37, L09605 <https://doi.org/10.1029/2010GL043227>.
- Bunting, M.J., Middleton, D., 2005. Modelling pollen dispersal and deposition using HUMPOL software, including simulating windroses and irregular lakes. *Rev. Paleobot. Palynol.* 134, 185–196.
- Bradtko, K., 2021. Landsat 8 data as a source of high resolution sea surface temperature maps in the Baltic Sea. *Remote Sens.* 13 (22), 4619. <https://doi.org/10.3390/rs13224619>.
- Chrysagi, E., Umlauf, L., Holtermann, P., Klingbeil, K., Burchard, H., 2021. High-resolution simulations of submesoscale processes in the Baltic Sea: the role of storm events. *J. Geophys. Res. Oceans* e2020JC016411. <https://doi.org/10.1029/2020JC016411>.
- Gordon, H.R., Morel, A., 1983. In: *Remote Assessment of Ocean Color for Interpretation of Satellite Visible Imagery: A Review*. Springer-Verlag, New York, p. 114.
- Hu, C., 2021. Remote detection of marine debris using satellite observations in the visible and near infrared spectral range: challenges and potentials. *Remote Sens. Environ.* 259, 112414 <https://doi.org/10.1016/j.rse.2021.112414>.
- Hu, C., 2022. Remote detection of marine debris using Sentinel-2 imagery: a cautious note on spectral interpretations. *Mar. Pollut. Bull.* 183, 114082 <https://doi.org/10.1016/j.marpolbul.2022.114082>.
- Hu, C., Qi, L., Xie, Y., Zhang, S., Barnes, B.B., 2022. Spectral characteristics of sea net reflectance observed from satellites: implications for remote sensing of marine debris. *Remote Sens. Environ.* 269, 112842 <https://doi.org/10.1016/j.rse.2021.112842>.
- Kahru, M., Elmgren, R., Savchuk, O.P., 2016. Changing seasonality of the Baltic Sea. *Biogeosciences* 13, 1009–1018. <https://doi.org/10.5194/bg-13-1009-2016>.
- Kahru, M., Elmgren, R., Kaiser, J., Wasmund, N., Savchuk, O., 2020. Cyanobacterial blooms in the Baltic Sea: correlations with environmental factors. *Harmful Algae* 92, 101739. <https://doi.org/10.1016/j.hal.2019.101739>.
- Kowalczyk, P., Darecki, M., Zablocka, M., Górecka, I., 2010. Validation of empirical and semi-analytical remote sensing algorithms for estimating absorption by coloured dissolved organic matter in the Baltic Sea from SeaWiFS and MODIS imagery. *Oceanologia* 52 (2), 171–196. <https://doi.org/10.5697/oc.52-2.171>.
- Kruse, F.A., Lefkoff, A.B., Boardman, J.W., Heidebrecht, K.B., Shapiro, A.T., Barloon, P. J., Goetz, A.F.H., 1993. The spectral image processing system (SIPS)—interactive visualization and analysis of imaging spectrometer data. *Remote Sens. Environ.* 44, 145–163.
- Lienart, C., Cirtwill, A.R., Hedgespeth, M.L., Bradshaw, C., 2022. A sprinkling of gold dust: pine pollen as a carbon source in Baltic Sea coastal food webs. *Limnol. Oceanogr.* 67, 53–65. <https://doi.org/10.1002/lno.11974>.
- Lu, Y., Shi, J., Hu, C., Zhang, M., Sun, S., Liu, 2020. Optical interpretation of oil emulsions in the ocean – Part II: applications to multi-band coarse-resolution imagery. *Remote Sens. Environ.* 242, 111778 <https://doi.org/10.1016/j.rse.2020.111778>.
- Mélin, F., Zibordi, G., 2010. Vicarious calibration of satellite ocean color sensors at two coastal sites. *Appl. Opt.* 49 (5), 798–810.

- Miettinen, A., Rinne-Garmston, J.T., Haila, H., Hyvarinen, H., 2002. The marine Eemian of the Baltic: new pollen and diatom data from Peski, Russia, and Põhja-Uhtju, Estonia. *J. Quat. Sci.* 17, 445–458. <https://doi.org/10.1002/jqs.706>.
- Mikelsons, M., Wang, M., 2018. Interactive online maps make satellite ocean data accessible. *Eos* 99. <https://doi.org/10.1029/2018EO096563>.
- Morel, A., Prieur, L., 1977. Analysis of variations in ocean color. *Limnol. Oceanogr.* 22 (4), 709–722.
- Muller-Karger, F.E., Varela, R., Thunell, R., Luerssen, R., Hu, C., Walsh, J.J., 2005. The importance of continental margins in the global carbon cycle. *Geophys. Res. Lett.* 32, L01602 <https://doi.org/10.1029/2004GL023146>.
- Onken, R., Baschek, B., Angel-Benavides, I.M., 2020. Very high-resolution modeling of submesoscale turbulent patterns and processes in the Baltic Sea. *Ocean Sci.* 16 (3), 657–684. <https://doi.org/10.5194/os-16-657-2020>.
- Ostrowska, M., Ficek, D., Stoltmann, D., Stoń-Egiert, J., Zdun, A., Kowalewski, M., Zapadka, T., Majchrowski, R., Pawlik, M., Dera, J., 2022. Ten years of remote sensing and analyses of the Baltic Sea primary production (2010–2019). *Remote Sens. Appl. Soc. Environ.* 26, 100715 <https://doi.org/10.1016/j.rsase.2022.100715>.
- Pawlik, M., Ficek, D., 2016. Pine pollen grains in coastal waters of the Baltic Sea. *Int. J. Oceanogr. Hydrobiol.* 45, 35–41. <https://doi.org/10.1515/ohs-2016-0004>.
- Pawlik, M., Ficek, D., 2021. Validation of measurements of pine pollen grain concentrations in Baltic Sea waters. *Oceanologia*. <https://doi.org/10.1016/j.oceano.2021.11.001>.
- Qi, L., Hu, C., Mikelsons, K., Wang, M., Lance, V., Sun, S., Barnes, B.B., Zhao, J., der Zande, D.V., 2020. In search of floating algae and other organisms in global oceans and lakes. *Remote Sens. Environ.* 239, 111659 <https://doi.org/10.1016/j.rse.2020.111659>.
- Qi, L., Hu, C., 2021. To what extent can Ulva and Sargassum be detected and separated in satellite imagery? *Harmful Algae* 103, 102001. <https://doi.org/10.1016/j.hal.2021.102001>.
- Qi, L., Tsai, S-F., Chen, Y., Le, C., Hu, C., 2019. In search of red Noctiluca scintillans blooms in the East China Sea. *Geophys. Res. Lett.* 46, 5997–6004. <https://doi.org/10.1029/2019GL082667>.
- Qi, L., Yao, Y., English, D.E., Ma, R., Luft, J., Hu, C., 2021. Remote sensing of brine shrimp cysts in salt lakes. *Remote Sens. Environ.* 266, 112695 <https://doi.org/10.1016/j.rse.2021.112695>.
- Reinart, A., Kutser, T., 2006. Comparison of different satellite sensors in detecting cyanobacterial bloom events in the Baltic Sea. *Remote Sens. Environ.* 102, 74–85.
- Rösel, S., Rychła, A., Wurzbacher, C., Grossart, H.-P., 2012. Effects of pollen leaching and microbial degradation on organic carbon and nutrient availability in lake water. *Aquat. Sci.* 74, 87–99. <https://doi.org/10.1007/s00027-011-0198-3>.
- Schiewer, U., 2008. Chapter 2: the Baltic coastal zones. In: *Ecology of Baltic Coastal Waters*. Springer. <https://doi.org/10.1007/978-3-540-73524-3>.
- Sugita, S., 1993. A model of pollen source area for an entire lake surface. *Quat. Res.* 39 (2), 239–244.
- Van Wirdum, F., Andren, E., Wienholz, D., et al., 2019. Middle to late Holocene variations in salinity and primary productivity in the Central Baltic Sea: a multiproxy study from the Landsort Deep. *Front. Mar. Sci.* 6, 51. <https://doi.org/10.3389/fmars.2019.00051>.
- Woźniak, S.B., Darecki, M., Zabłocka, M., Burska, D., Dera, J., 2016. New simple statistical formulas for estimating surface concentrations of suspended particulate matter (SPM) and particulate organic carbon (POC) from remote-sensing reflectance in the southern Baltic Sea. *Oceanologia* 58 (3), 161–175. <https://doi.org/10.1016/j.oceano.2016.03.002>.
- Zhang, W., Harff, J., Schneider, R., 2011. Analysis of 50-year wind data of the southern Baltic Sea for modelling coastal morphological evolution – a case study from the Darss-Zingst Peninsula. *Oceanologia* 53, 489–518.
- Zibordi, Berthon, G.J.-F., Mélin, F., D'Alimonte, D., Kaitala, S., 2009. Validation of satellite ocean color primary products at optically complex coastal sites: Northern Adriatic Sea, northern Baltic Proper, Gulf of Finland. *Remote Sens. Environ.* 113, 2574–2591.
- Ziska, L.H., Caulfield, F.A., 2000. Rising CO₂ and pollen production of common ragweed (*Ambrosia artemisiifolia* L.), a known allergy-inducing species: implications for public health. *Aust. J. Plant Physiol.* 27 (10), 893–898.